Geochemistry Geophysics Geosystems G3

Article
Volume 14, Number 7
29 July 2013
doi: 10.1002/ggge.20155
ISSN: 1525-2027

Published by AGU and the Geochemical Society

Dynamics of outer-rise faulting in oceanic-continental subduction systems

John B. Naliboff
Department of Geology, University of California, Davis, California, USA (jbnaliboff@ucdavis.edu)

Magali I. Billen
Department of Geology, University of California, Davis, California, USA

Taras Gerya
Geophysical Fluid Dynamics Group, Institute of Geophysics Department of Earth Sciences, Swiss Federal Institute of Technology, Zurich, Switzerland

Jessie Saunders
Department of Geology, University of California, Davis, California, USA

[1] During subduction, bending of downgoing oceanic lithosphere gives rise to normal faulting due to the extensional stress state generated in the upper plate. As deformation patterns inherently reflect a material's state of stress and rheology, extensive global observations of outer-rise faulting patterns and subduction dynamics provide a unique opportunity to examine the factors controlling outer-rise deformation. Despite a wide range of observed oceanic plate ages, convergence rates and slab pull magnitudes across modern subduction systems, however, measured outer-rise faulting patterns show effectively no correlation to variations in these parameters. This lack of correlation may reflect that outer-rise faulting patterns are strongly sensitive to all of these parameters, are dependent on additional parameters such as downgoing-overriding plate coupling or that existing faulting measurements require additional analysis. In order to provide a basis for future analysis of outer-rise faulting patterns, we build on previous thermo-mechanical numerical models of outer-rise deformation and explore the relationship between outer-rise faulting patterns, subduction dynamics and brittle rheology in an oceanic-continental subduction system. Analysis of time-averaged outer-rise faulting patterns indicates that downgoing plate age and velocity, downgoing-overriding plate coupling and slab pull all significantly affect faulting patterns, while variations in brittle rheology have a significantly smaller impact. These relationships reflect that the sensitivity of outer-rise faulting patterns to the frictional properties of the oceanic crust and mantle is small compared to variations in the overall stress state and deformation rate of subduction systems. In order to gain additional insight into the origin outer-rise faulting patterns, future numerical studies should focus on specific regions in order to place constraints on the structure of the downgoing plate and dynamics of the subduction system.

Components: 9,895 words, 9 figures, 2 tables.

Keywords: oceanic-continental subduction; outer-rise faulting; lithospheric rheology.

Index Terms: 8170 Tectonophysics: Subduction zone processes; 8120 Tectonophysics: Dynamics of lithosphere and mantle: general; 8159 Tectonophysics: Rheology: crust and lithosphere; 8155 Tectonophysics: Plate motions: general.

Received 11 December 2012; **Revised** 19 April 2013; **Accepted** 24 April 2013; **Published** 29 July 2013.

Naliboff, J. B., M. I. Billen, T. Gerya, and J. Saunders (2013), Dynamics of outer-rise faulting in oceanic-continental subduction systems, *Geochem. Geophys. Geosyst., 14,* 2310–2327, doi:10.1002/ggge.20155.

1. Introduction

[2] During subduction, bending and flexure of downgoing oceanic lithosphere generates a topographic bulge seaward of the trench known as the outer rise [e.g., *Parsons and Molnar*, 1976; *De Bremaecker*, 1977; *Turcotte et al*., 1978; *Melosh*, 1978]. Flexure of the downgoing plate also generates significant bending stresses, which grade from extensional at the top of the plate to compressional at the base. Active normal faulting within the outer-rise region [e.g., *Ludwig et al*., 1966; *Jones et al*., 1978; *Hilde*, 1983; *Masson*, 1991; *Kobayashi et al*. 1998; *Massell*, 2002; *Mortera-Gutierrez et al*., 2003; *Ranero et al*., 2003, 2005; *Oakley et al*., 2008; *Lefeltd et al*., 2012] reflects the brittle rheologic response of the oceanic lithosphere to these extensional bending stresses and the pull of previously subducted lithosphere within the upper mantle (i.e., slab-pull force). Outer-rise faults are either reactivated abyssal-hill fault or new faults, formed within 40–75 km of the trench, spaced 1–10 km apart [*Masson*, 1991] and extending deep into the mantle portion of the subducting plate [e.g., *Ranero et al*., 2003]. Although the size and magnitude of such faulting within the outer rise is second-order in comparison to motion along the subducting plate interface, the resulting deformation of the downgoing plate significantly influences seismogenic and long-term geodynamic processes.

[3] On the seismogenic timescale, outer-rise faulting is both a source of large magnitude earthquakes [*Lynnes and Lay*, 1988, for example] and an indicator of the seismic potential for large underthrusting events [*Christensen and Ruff*, 1988]. Repeated seismogenic deformation along outer-rise faults also provides potential pathways for fluid migration due to weakening along the fault interfaces. Indeed, recent observational [*Ranero et al*., 2003; *Ranero and Sallares*, 2004; *Ranero et al*., 2005; *Grevemeyer et al*., 2005, 2007; *Tilmann et al*., 2008; *Syracuse et al*., 2008; *Ivandic et al*., 2010; *Key et al*., 2012; *Lefeltd et al*., 2012] and numerical [*Faccenda et al*., 2009, 2012] studies suggest that outer-rise faults may act as active conduits for fluid transport deep into slabs, which in turn may both significantly reduce the strength of hydrated slab rocks [e.g., *Hirth and Kohlstedt*, 1996; *Escartin et al*., 1997a; *Floyd et al*., 2001] and provide a mechanism for recycling of volatiles into the deep mantle [*Faccenda et al*., 2009, 2012].

[4] On longer time scales, weakening due to faulting, fluid alteration or plastic yielding in the outer-rise region [*Billen and Gurnis*, 2005; *Contreras-Reyes and Osses*, 2010; *Arredondo and Billen*, 2012] directly influences large-scale subduction processes. Weakening in the outer rise affects the amount of energy dissipated during bending of the slab [e.g., *Conrad and Hager*, 1999, 2001; *Becker et al*., 1999; *Buffett*, 2006; *Di Giuseppe et al*., 2008; *Schellart*, 2009; *Capitanio et al*., 2009; *Leng and Zhong*, 2010; *Stadler et al*., 2010; *Rose and Korenaga*, 2011; *Buffet and Becker*, 2012] and the coupling (i.e., slab-pull) between the surface plate and subducted material in the upper mantle, which in turn affects the available forces to drive plates through slab pull and suction [e.g., *Conrad and Lithgow-Bertelloni*, 2002; *Wu et al*., 2008; *Capitanio et al*., 2009; *van Summeren et al*., 2012; *Alisic et al*., 2012]. In turn, a reduction in the magnitude of slab-pull through weakening of the downgoing plate may reduce the rate or distribution of faulting in the outer rise as extensional stress magnitudes decrease. Such a relationship provides a direct feedback mechanism between large-scale subduction dynamics and normal faulting in the outer-rise region, which depends on the structure of the downgoing plate, the rheological properties of the oceanic lithosphere and the time-dependent evolution of the subduction dynamics. While recent models [*Faccenda et al*., 2012] have closely examined the relationship between outer-rise faulting patterns, seismic anisotropy, and water transport into the deep mantle, no studies exist that quantify how outer-rise faulting patterns vary over a range of the above parameters.

[5] Furthermore, measurements of outer-rise fault spacing and extent show little to no correlation with incoming plate age, convergence velocity and slab pull magnitude (Table 1), which all affect the bending mechanics and stress state in the outer-rise region to various degrees [e.g., *Buffett*, 2006; *Capitanio et al*., 2007, 2009; *Di Giuseppe et al*., 2008; *Rose and Korenaga*, 2011; *Buffett and Becker*, 2012; and references therein]. Indeed, the lack of correlation between outer-rise faulting measurements, subducting plate age and convergence velocity was noted by *Masson* [1991], although more recent measurements [e.g., *Massell*, 2002; *Ranero et al*., 2003; *Oakley et al*., 2008; this study] have not resolved this discrepancy (Table 1). Notably, within a single subduction system outer-rise faulting patterns often vary

Table 1. Outer-Rise Faulting Patterns and Subduction Characteristics for Multiple Regions

Name	Approximate Measurement Location	Fault Spacing (km)	Lateral Faulting Extent (km)	Plate Age (Myr)[g]	Convergence Rate (cm/yr)[g]	Slab Pull (10^{12} N/m)[g]
Peru[a]	10–14°S	1–15	50–75	46	6.8	29–30
Java[a]	108–120°E	2–10	50	80–84	6.0–6.6	25–26
Izu-Bonin[a]	33–35°N	1–10	50	129	5.5	36
Japan[a]	36–40.5°N	2–10	50	127–132	9.0–9.3	50–62
Aleutian[a]	170°E–179°W	1–10	40–75	39–63	2.1–6.5	10–18
Costa Rica[b]	9.75–10.9°N	2.14, 1.58	25.18, 6.99	26	8.3	10
Costa Rica[c]	10–11°N	1.80, 0.91[d]	25[d]	26	8.3	10
N. Chile[e]	21–24°S	2–5	40–50	53–55	7.1–7.2	28–29
Tonga[b]	16.75–21.52°S	2.41, 2.02	44.27, 7.47	14.8–18.3	107–108	30–31
Marianas[f]	16.7–17.9°N	7.84, 6.38	68.86, 10.98	150–153	5.9–6.9	31
Izu-Bonin[f]	30.9–32.3°N	9.19, 4.75	86.18, 9.02	129–135	5.1	33
Kurile[b]	41.43–41.99°N	2.93, 2.33	41.35, 11.04	128	7.7	50

[a]Data from *Masson* [1991].
[b]Data collected for this study [see supplementary information].
[c]Data collected from *Ranero et al*. [2003].
[d]Data from *Ranero et al*. [2003] is restricted to faulting within 25 km of the trench.
[e]Data from *Massell* [2002].
[f]Data from *Oakley* [2008].
[g]Data from *Lallemand et al.* [2005].

significantly along strike (trench-parallel) and along the extent of the trench wall (trench-perpendicular) [e.g., *Massell*, 2002; *Ranero et al*., 2003, 2005; *Mortera-Gutierrez et al*., 2003; *Oakley et al*., 2008]. In addition, the faulting measurements in Table 1 do not distinguish between reactivated and newly formed faults, with the exception of data from Northern Chile [*Massell*, 2002]. Reactivated faults may be up to 30% weaker (lower coefficient of friction) than new faults [*Billen et al*., 2007], which is expected to affect the stress (location) at which they are reactivated, as well as their spacing and size. As such, a more detailed analysis of global outer-rise faulting patterns may reveal relationships masked within the present data (Table 1). Alternatively, additional factors such as coupling across the plate boundary interface [e.g., *Gerya and Meilick*, 2011; *Tan et al*., 2012] may also strongly influence subduction dynamics and outer-rise deformation patterns, thus requiring a more sophisticated multivariate analysis.

[6] The primary goal of this study is to carefully examine the various factors controlling outer-rise deformation patterns in order to provide a basis for future analysis of outer-rise faulting patterns at both global and regional scales. Building off of previous 2-D numerical models, we quantify the relationship between oceanic plate age, velocity, downgoing-overriding plate coupling, slab-pull and brittle strength on outer-rise faulting in an oceanic-continental subduction system. We find that downgoing-overriding plate coupling and subducting plate structure and velocity exert a clear, first-order control on normal faulting patterns in the outer-rise region, while the effects of brittle strength are comparatively subtle and difficult to detect.

2. Computational Methods

2.1. Numerical Design, Boundary Conditions, Geologic Domains and Melting

[7] We model thermal-mechanical deformation in the outer-rise region of a 2-D oceanic-continental subduction system using the conservative finite-difference, particle-in-cell code I2ELVIS [*Gerya and Yuen*, 2007]. Our numerical setup follows that of previous oceanic-continental subduction systems modeled using I2ELVIS [*Gorczyk et al*., 2007; *Nikolaeva et al*., 2010; *Gerya and Meilick*, 2011; *Vogt et al*., 2012], which contain additional details on the implementation of boundary conditions, melting and fluid transport.

[8] The computational domain spans 2000 km and 200 km (or 600 km), respectively, in the horizontal and vertical directions (Figure 1). Numerical resolution varies spatially, and ranges from 2 km up to 0.5 km in the vicinity of the trench. Notably, a resolution of 0.5 km was used in previous similar studies [*Faccenda et al*., 2008, 2009] and additional testing of models with a 0.25 km confirmed the robustness of our results. The top and sides of the model maintain a zero shear stress (free-slip) boundary condition, while the bottom boundary contains an external no slip condition that allows material to flow through the base and still satisfy global conservation of mass [see *Gorczyk et al*.,

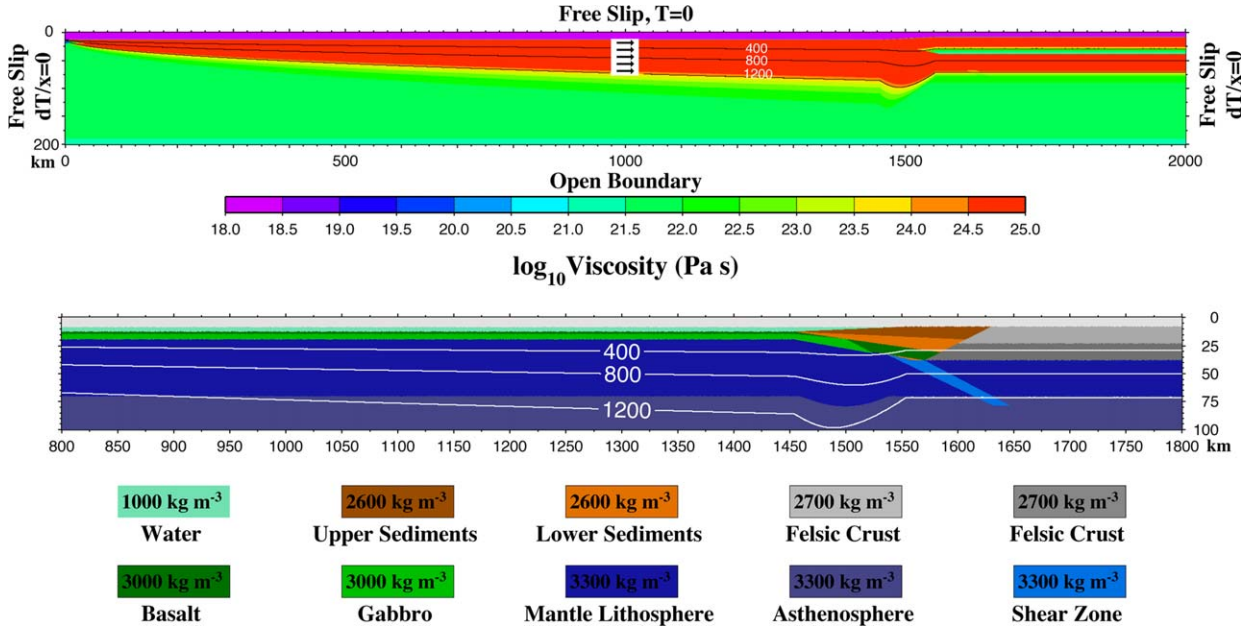

Figure 1. Numerical setup and initial conditions of 2-D thermo-mechanical model. Top: initial viscosity structure with temperature (°C) contours. The top and side boundaries are free-slip, while the bottom boundary is open with flow-rate constrained by an external no-slip condition. An internal velocity driving subduction is applied along the oceanic lithosphere at a horizontal position of 1000 km (white box with arrows). Temperature is fixed (0°C) at the top of the model, while the sides permit zero heat flux and the bottom maintains an external thermal boundary. Bottom: initial composition structure with temperature contours.

2007; *Gerya and Meilick*, 2011]. The bottom boundary also maintains an external thermal boundary, while the top boundary remains fixed at 0 °C and the model sides permit zero heat flux. Within the oceanic lithosphere 1000 km from the left edge, a fixed velocity field over the thickness of the plate drives subduction (Figure 1). In contrast to previous studies of outer-rise deformation [*Faccenda et al*., 2009, 2012], we maintain this applied velocity throughout the model simulations in order to ensure a relatively consistent rate of subduction.

[9] Internally, thermal, compositional, and rheological variations define distinct geologic domains (Figure 1, Table 2). At the surface, rheologically weak air (0–8 km depth, 1 kg m^{-3}) and water (8–12.5 km depth, 1000 kg m^{-3}) layers decouple the underlying lithosphere from the top free-slip boundary, which allows the lithosphere surface to behave as a quasi free-surface [e.g., *Schmeling et al*., 2008]. The boundary between the lithosphere and air/water evolves through erosion and sedimentation via the transport equation [e.g., *Gerya and Yuen*, 2003a; *Gorzyck et al*. 2007]. Both the air and water layers maintain a fixed temperature of 0°C.

[10] The oceanic and continental lithosphere, respectively, are defined by half-space [e.g., *Turcotte and Schubert*, 2002] and linear cooling models, where the continental geotherm grades from 0 to 1402°C. The oceanic lithosphere thickens from the left side of the model (thickness ~ 0 km, age = 0 Myr) toward the oceanic-continental lithosphere boundary (Figure 1), where the maximum thickness is determined by a specified plate age. The oceanic and continental lithosphere contain compositionally and rheologically distinct crustal and mantle components, while a rheologically weak shear zone and water-saturated sediments at the oceanic-continental boundary help enable the initiation of subduction and prevent unrealistic coupling at the plate boundary (Figure 1 and Table 2). The asthenosphere extends from the base of the lithosphere to the model base, with an initial adiabatic geothermal gradient of 0.5°C per km. At all points within the lithosphere and asthenosphere, the mineral assemblage and corresponding water content is determined according to thermodynamic phase relations (P, T, C dependent), which accounts for such processes as phase changes, dehydration reactions and melting [e.g., *Gerya and Yuen*, 2003a, 2003b; *Connolly*,

Table 2. Reference Model Material Properties

Material	Solid Density (kg m^{-3})	Flow Law[a]	Friction Coefficient
Sediments	2600	Wet quarzite	$\sin\phi_{strong} = 0.15$ $\sin\phi_{weak} = 0.075$
Upper continental crust	2700	Wet quarzite	$\sin\phi_{strong} = 0.15$ $\sin\phi_{weak} = 0.075$
Lower continental crust	2700	Wet quarzite	$\sin\phi_{strong} = 0.15$ $\sin\phi_{weak} = 0.075$
Upper oceanic crust (basalt)	3000	Wet quartzite	$\sin\phi_{strong} = 0.15$ $\sin\phi_{weak} = 0.075$
Lower oceanic crust (gabbro)	3000	Plagioclase (An_{75})	$\sin\phi_{strong} = 0.6$ $\sin\phi_{weak} = 0.3$
Dry mantle (lithosphere-asthenosphere)	3300	Dry olivine	$\sin\phi_{strong} = 0.6$ $\sin\phi_{weak} = 0.3$
Wet mantle (lithosphere-asthenosphere)	3300	Wet olivine	$\sin\phi_{strong} = 0.1$ $\sin\phi_{weak} = 0.05$

[a]Flow laws taken from *Ranalli* [2005].

2005; *Gerya et al.*, 2006; *Gerya and Meilick*, 2011]

[11] Partial melting of dry and hydrated solid phases occurs at both the mid-ocean ridge and within the subduction zone according to defined thermodynamic phase relations [for specific details see *Gerya and Yuen*, 2003a, 2003b; *Connolly*, 2005; *Gerya et al.*, 2006; *Gerya and Yuen*, 2007; *Gorzyck et al.*, 2007; *Gerya and Meilick*, 2011; *Vogt et al.*, 2012]. Notably, melting only affects outer-rise deformation via weakening of the overriding plate and subsequent changes in trench dynamics as the rate of back-arc extension increases [*Gerya and Meilick*, 2011; *Vogt et al.*, 2012]. As such, we hold melting related parameters constant.

2.2. Water Content and Transport

[12] Models contain both molecular and connate water in the oceanic and continental lithosphere, with connate water restricted to basalt and continental sediment layers. The proportion of molecular water is based on the equilibrium mineralogical assemblages for each defined material [*Gerya and Meilick*, 2011], while the initial amount of connate water in oceanic basalt is varied from 0 to 2 wt. % (1 wt. % in reference model) to assess its effect on outer-rise faulting patterns. Continental sediments initially contain 1 wt. % connate water in all models. In order to account for dehydration reactions and the compaction of pore fluid space, connate water is progressively released with depth in the majority of models such that 0 wt. % is left at 75 km:

$$X_{H_2O(wt\%)} = (1 - 0.013 \cdot \Delta y) \cdot X_{H_2O(p0)}, \quad (1)$$

where Δy is the depth below the model surface and $X_{H_2O(p0)}$ is the initial water concentration in the oceanic lithosphere.

2.3. Rheology

[13] Deformation occurs through a combination of viscous flow and plastic yielding in the lithosphere, while asthenosphere, air and water layers are limited to viscous deformation (Table 1). In the lithosphere and asthenosphere, viscous flow occurs through dislocation creep defined by a temperature and strain-rate power law creep model:

$$\mu_{creep} = \frac{(\dot{\varepsilon}_{II})^{\frac{1-n}{n}}}{(A_D)^{\frac{1}{n}} \exp\left(\frac{E}{nRT}\right)}, \quad (2)$$

where $\dot{\varepsilon}_{II}$ is the second invariant of strain rate tensor, A_D pre-exponential factor, E activation energy, n creep exponent, R gas constant, and T temperature. Crustal and mantle portions of the continental and oceanic lithosphere are assigned unique experimentally determined values of E, A_D, and n from *Ranalli* [1995]. Air and water layers maintain a fixed viscosity 10^{18} Pa s.

[14] Brittle deformation occurs in the upper portions of the lithosphere through a Drucker-Prager yield criterion. This criterion establishes a yield stress (σ_{yield}) that limits stress magnitudes by reducing the material viscosity (μ) when the second deviatoric stress invariant (σ_{II}) exceeds the yield stress:

$$\text{if } \sigma_{II} > \sigma_{yield}, \mu = \frac{\sigma_{yield}}{2\dot{\varepsilon}_{II}}. \quad (3)$$

[15] Consequently, brittle deformation patterns largely reflect the magnitude of the yield stress, which is based on the dynamic pressure (P) and a material's cohesion (C, residual brittle strength at $P = 0$) and internal friction angle (φ):

$$\sigma_{yield} = C + \sin(\varphi)P. \quad (4)$$

[16] The friction coefficient depends on the total brittle strain ($\varepsilon_{brittle}$) accumulation, which we classify as low ($\varepsilon_{strong} = 0$) or high strain ($\varepsilon_{weak} = 1$):

$$\sin\varphi = \sin\varphi_{\text{strong}} \text{ for } \varepsilon_{\text{brittle}} < \varepsilon_{\text{strong}} \quad (5)$$

$$\sin\varphi = \sin\varphi_{\text{strong}} + \left(\sin\varphi_{\text{strong}} - \sin\varphi_{\text{weak}}\right) \frac{\varepsilon_{\text{brittle}}}{\varepsilon_{\text{brittle}} - \varepsilon_{\text{weak}}} \text{ for } \varepsilon_{\text{strong}} < \varepsilon_{\text{brittle}} < \varepsilon_{\text{weak}} \quad (6)$$

$$\sin\varphi = \sin\varphi_{\text{weak}} \text{ for } \varepsilon_{\text{brittle}} > \varepsilon_{\text{weak}} \quad (7)$$

where $\sin\varphi_{\text{weak}}$ and $\sin\varphi_{\text{strong}}$ are, respectively, the minimum and initial friction coefficient values (Table 1). In the presence of free water, the friction coefficient computed for dry rocks decreases linearly based on a fluid weakening parameter (λ_{fluid}):

$$\sin(\varphi) = \sin\left(\varphi_{\text{dry}}\right)\lambda_{\text{fluid}}. \quad (8)$$

[17] The fluid weakening parameter remains fixed at 0.1 and has little effect on faulting patterns in the outer rise due to the release of free water particles as a function of depth. Cohesion values are calculated in an equivalent fashion to the friction coefficient for dry and wet rocks, although we hold strong ($C_{\text{strong}} = 10$ MPa) and weak ($C_{\text{weak}} = 1$ MPa) values constant throughout in order focus on the effects of variations in the friction coefficient.

2.4. Faulting Pattern, Bending Radius, and Trench Velocity Analysis

[18] Quantitative measures of faulting patterns are determined through analysis of viscosity profiles along the downgoing plate (Figure 2). As the oceanic lithosphere descends, brittle deformation is accommodated by low-viscosity (high-strain rate) shear bands (i.e., faults), which follow the plate curvature (Figure 2a). In order to analyze faults along a plane consistent with plate curvature, viscosity profiles (Figure 2b) are extracted along a curve (Figure 2a, lower black curve) parallel to and 3 km beneath the Moho (Figure 2a, upper black curve). Faulting analysis is restricted to the mantle lithosphere to avoid the presence of numerous small and discontinuous faults in the oceanic crust, particularly down-dip of the trench. Viscosity minimums along each profile mark the center of faults (blue diamonds in Figure 2a), which are identified through an automated search procedure. Subsequent manual steps remove erroneous points and add any unidentified faults (typically near fault intersections).

[19] Each recorded fault contains a record of its spatial coordinates, dip-direction and viscosity, allowing for additional filtering and classification steps. For example, a specified maximum fault viscosity limits the total number of faults (5×10^{23} Pa s in Figure 2b). At each time step, faulting patterns are described in terms of their number, lateral extent and position relative to the trench (Figure 2b). The lateral extent of faulting measures the total distance along the Moho parallel curve from the first to last fault, while the trench-faulting offset measures the horizontal distance from the trench to the last fault (Figure 2b). Fault spacing values represent the distance between adjacent faults (Figure 2b), while a fault spacing measurement reported for a specific time step represents the average fault spacing value. The shape of the downgoing slab is quantified in terms of the bending radius and minimum bending radius along the curve through the Moho (Figure 2a). The bending radius is determined by fitting a circle through three points along Moho at depths of 30, 70, and 140 km [e.g., Vogt et al., 2012]. The minimum bending radius is defined following the method of *Capitanio et al*. [2009]:

$$K = \frac{1}{R} = \frac{\frac{\partial^2 y}{\partial x^2}}{\sqrt{\left(1 + \left(\frac{\partial y}{\partial x}\right)^2\right)^3}} \quad (9)$$

where K is the curvature, R is the bending radius, and y and x, respectively, are the vertical and horizontal coordinates. Under this definition, the bending radius varies continuously along the slab and the minimum valued is used as a representative measure.

[20] Trench velocity is recorded at each time step using the maximum depth of the water layer (trench location) and the relative motion of this point through time. In the case of trench advance, the trench moves toward the right model boundary and has a positive velocity. In the case of trench retreat, the trench moves toward the left boundary and has a negative velocity.

3. Results

3.1. Reference Model

3.1.1. Downgoing and Overriding Plate Evolution

[21] To provide a basis for time-averaged analysis of faulting patterns, we first consider the temporal evolution of outer-rise deformation in an evolving subduction system. Brittle deformation in the downgoing plate (Myr) is accommodated by

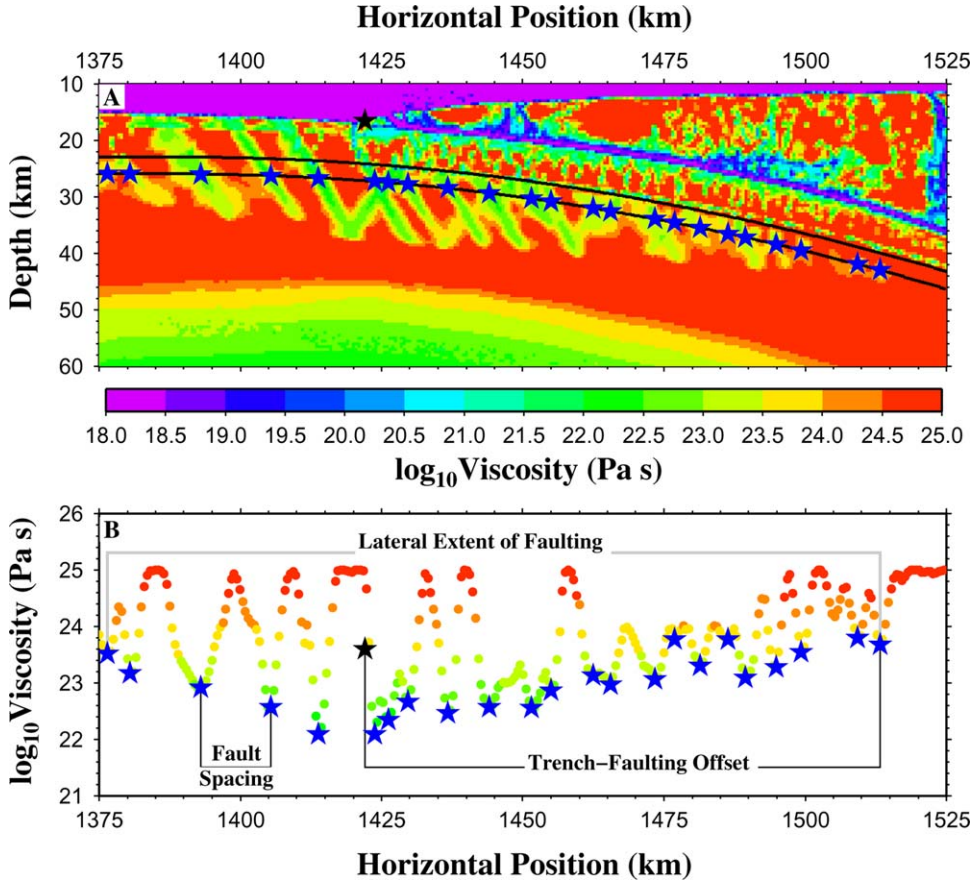

Figure 2. Reference model at time = 8.70 Myr. (a) Viscosity structure of the deforming oceanic lithosphere (plate age = 40 Myr) and sedimentary accretionary wedge. Low-viscosity shear zones develop as the downgoing plate bends beneath the trench. The curvature of the slab is mapped by fitting a curve through the Moho (upper black curve). Faults (i.e., shear zones) are classified within the mantle lithosphere along a profile parallel to and 3 km beneath the Moho (lower black curve). Blue stars represent the locations of faults determined from viscosity profiles along the lower black curve. (b) Profile of viscosity versus horizontal position along a curve 3 km beneath the Moho. Fault locations are classified as the lowest viscosity value within each shear zone. Lateral extent of faulting: distance from first (farthest left) to last (farthest right) fault. Trench-faulting offset: horizontal distance from last fault to the trench. Fault-spacing: distance between adjacent faults.

low-viscosity (high-strain rate) shear bands (i.e., faults), which extend laterally both seaward and down-dip of the trench for 10s of kilometers (Figure 3). Although seaward-dipping and antithetic faults do develop, the majority of faults dip trenchward, consistent with observations of outer-rise faulting [e.g., *Masson*, 1991] and previous numerical models [*Faccenda et al*., 2008, 2009]. Seaward of the trench, the largest faults are generally continuous from the plate surface to their termination near the midplane of the plate, which marks the transition from extension to compression (Figures 3f–3j). Down-dip of the trench, however, faults are largely discontinuous across the Moho, with deformation in the crust characterized by smaller and more tightly spaced faults. This pattern of deformation in the crust reflects the conversion of connate water into free water particles as the plate descends (equation (1)), which decreases the brittle strength of the crust (equation (8)). The documented decoupling of crustal and mantle faulting patterns inside the subducted slab is caused by the slab hydration through the faults [*Faccenda et al*., 2009], which creates a subcrustal rheologically weak serpentinized mantle layer that decouples crustal and mantle deformation. Faulting within the upper plate terminates at varying depths beneath the accretionary wedge as the yield stress increases with pressure (equation (4)) and eventually exceeds the extensional tectonic stress within the upper downgoing plate (Figures 3f–3j).

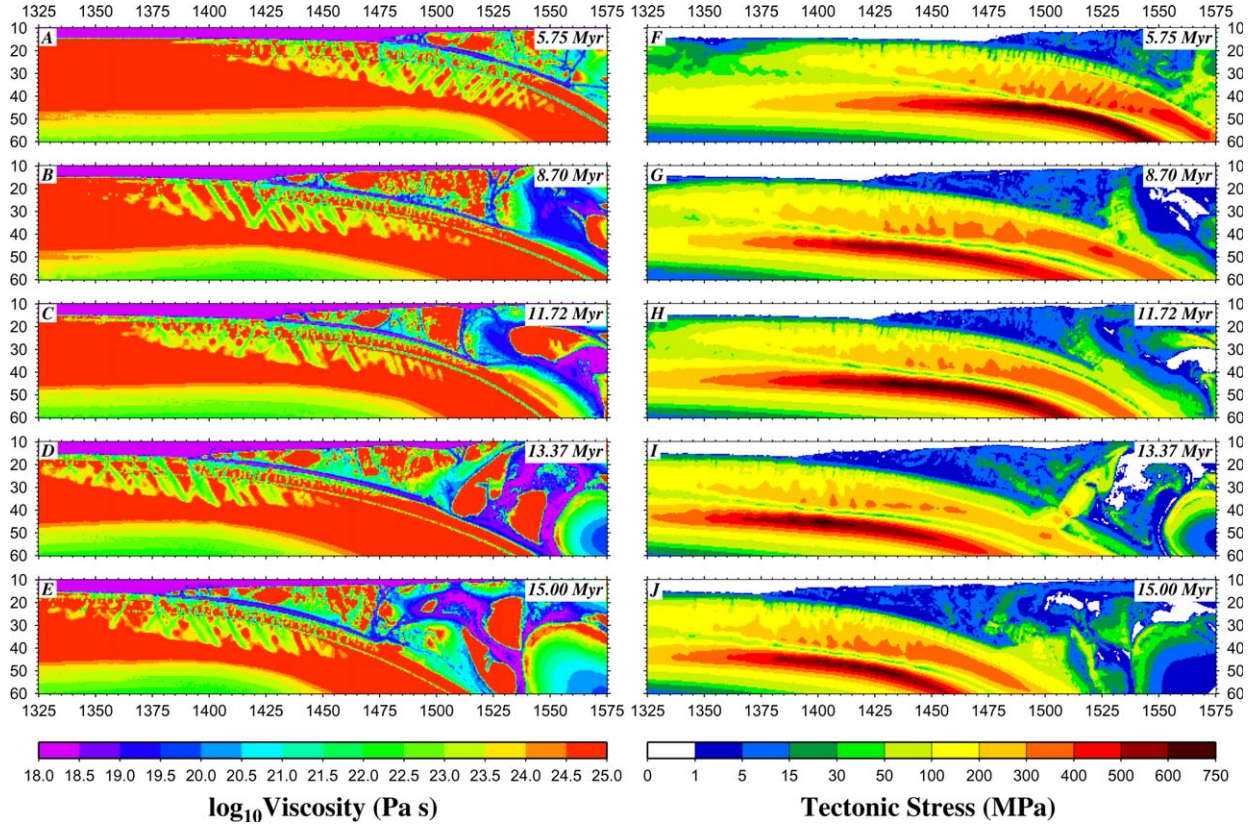

Figure 3. Viscosity (left column) and absolute tectonic stress (right column) with time (upper right corners) for the reference model, which has a spatial resolution of 500 m in the vicinity of the trench and an oceanic plate age of 40 Myr.

[22] The location and pattern of faulting varies with time as the oceanic lithosphere and overriding plate deforms. As subduction progresses, return flow in the mantle wedge drives deformation and eventual intra-arc spreading initiation in the overriding plate (Figure 3), which is significantly weakened by the presence of fluids and melt [e.g., *Gerya and Meilick*, 2011; *Vogt et al*., 2012]. Extension of the overriding plate increases the rate of trench retreat with time and modifies the stress state within the downgoing plate (Figure 3) through coupling (transmission of stress) across the plate boundary.

3.1.2. Faulting Patterns

[23] In order to assess the relative contribution of downgoing plate deformation and plate-boundary coupling to temporal variations in faulting patterns, we compare quantitative measures of faulting patterns to variations in trench velocity, trench position and bending radius at time-steps output on average every 0.58 Myr (Figure 4). Faulting patterns are subdivided between faults with maximum viscosities of 5×10^{23} and 5×10^{22} Pa s to test the robustness of any observed relationships. In general, lower maximum fault viscosities values identify the more robust and fully developed faults. Reducing the maximum fault viscosity from 5×10^{23} to 5×10^{22} Pa s has a significant impact on measured faulting patterns and decreases the number of observed faults (Figures 4a–4c) from a range of 15–25 to less than 10, while the lateral faulting extent (Figures 4d–4f) similarly decreases from $\sim$ 100–150 to $\sim$ 25–50 km. In contrast, faulting spacing (Figures 4g–4i) is comparatively unaffected by the maximum fault viscosity with the majority values ranging from 5 to 8.5 km.

[24] Plotted against bending radius, the number of faults and lateral faulting extent remain effectively constant across a range of values between 180 and 300 km, while fault spacing values are comparatively scattered. Similarly, faulting patterns exhibit a minimal dependence on trench velocity (Figure 4, middle column), although trench velocities are restricted to a small range of values (0–4 cm yr^{-1}) with the exception of one period fast trench retreat ($\sim$ 9 cm yr^{-1}). During this period of fast retreat all

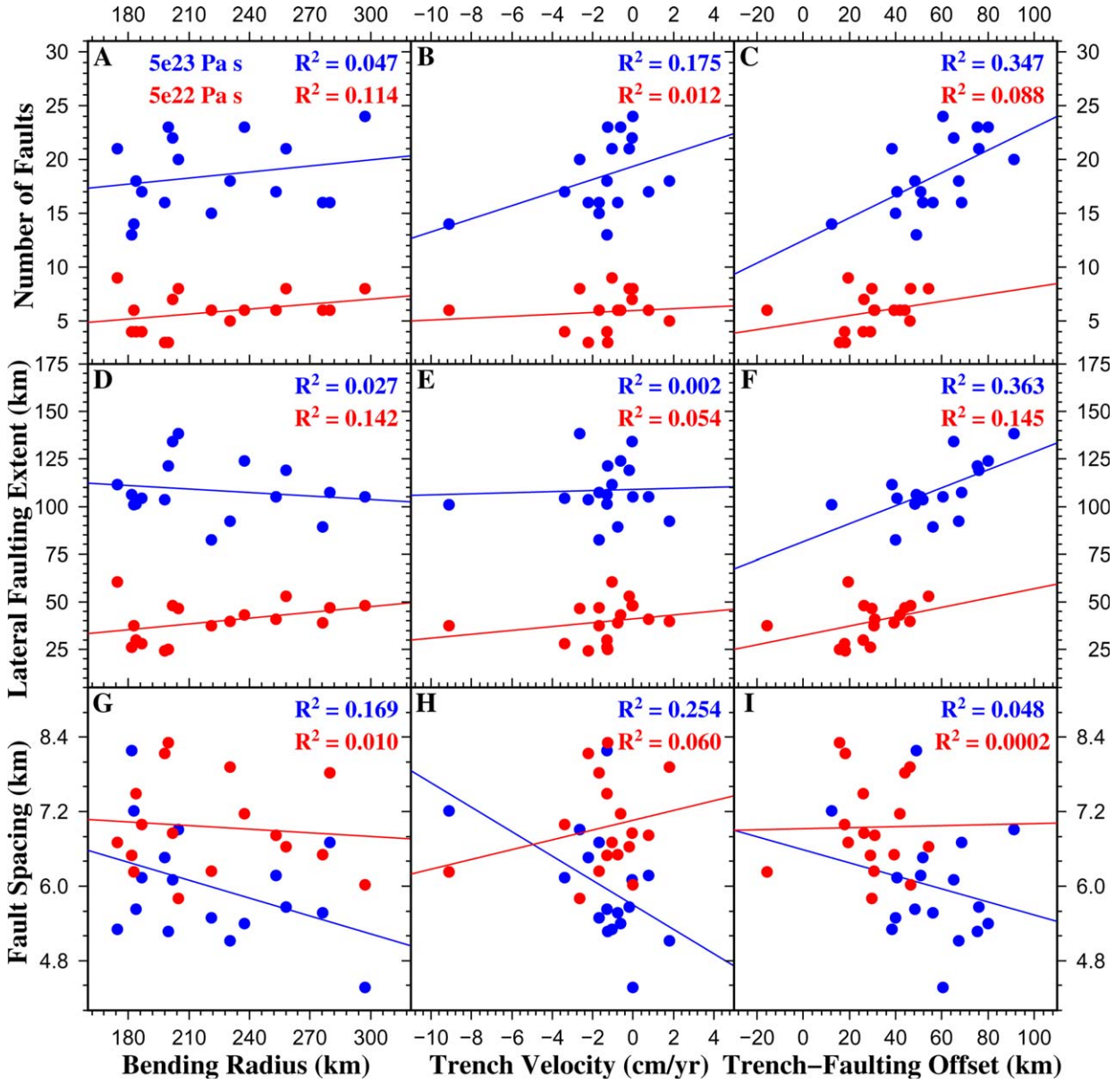

Figure 4. Reference model faulting patterns as a function of minimum bending radius, trench velocity and trench-faulting offset (distance between last measured faults and the horizontal position of the trench). Measured faults have a maximum viscosity of 5×10^{23} (blue) or 5×10^{22} (red) Pa s. The number of faults (top row), lateral faulting extent (middle row) and fault spacing (bottom row) are considered. Red and blue lines represent the best-fit line through each set of points, which are determined via linear regression. R^2 values represent the coefficient of determination for each best-fit line. Faulting properties are largely insensitive to the bending radius and trench velocity, but do show a correlation to the trench-faulting offset.

three measures of faulting plot well within the range of observed values, and do not reveal a strong dependence on the trench velocity.

[25] In contrast to minimum bending radius and trench velocity, faulting patterns exhibit a moderate correlation to the horizontal distance between the last measured fault and the location of the trench (Trench-Faulting Offset, Figure 4, right column), which ranges from 100 km (last fault 100 km down-dip of trench) to −20 km (last fault 20 km seaward of trench). The lateral faulting extent and number of faults both increase as the faulting zone moves toward or down-dip of the trench, which indicates that forces driving brittle deformation seaward also decrease the faulting extent and number of faults. Notably, fault spacing shows

little correlation with trench-faulting offset. This indicates that decreases or increases in the lateral extent of faulting are accompanied by similar changes in the number of faults, such that fault spacing remains roughly constant.

[26] These patterns reflect the balance in the overriding plate between bending, slab pull and extension of the overriding plate. As the overriding plate extends, compressional forces are transmitted across the plate boundary into the downgoing plate, which decreases the area beneath the trench where extensional stresses exceed the pressure-dependent yield stress. As the faulting zone migrates seaward due to increasing compression across the plate boundary interface, the number and lateral extent of faulting correspondingly decreases.

[27] While direct comparisons of the above results to specific subduction zones are difficult due in part to the processes described above, lateral faulting extent (100–150 km) and fault spacing (5–8.5 km) measurements should fall within the bounds of compiled global observations (Table 1) if the models accurately capture the dynamics of outer-rise deformation. Indeed, the results fall well within global ranges of fault spacing (1–10 km) and lateral faulting extent (40–75 km) [*Masson*, 1991], with lateral faulting extent observations representing the distance from the trench to the beginning of faulting, such that they should be approximately half of our reported values. Notably, fault spacing may vary along strike and as a function of distance from the trench [e.g., *Ranero et al*., 2003, 2005; *Massell*, 2002; *Mortera-Gutierrez et al*., 2003; *Oakley et al*., 2008], with the latter observation being consistent with our models for individual time-steps (Figure 2) and time-dependent patterns (Figures 3 and 4). As the reference model faulting patterns fall well within global constraints, we are confident in expanding our experiments to examine additional parameters influencing outer-rise deformation.

[28] Prior to proceeding, it should be noted that patterns of brittle deformation are highly sensitive to numerical resolution [e.g., *Buiter et al*., 2006], and thus our results also depend on the ability of the model to resolve shear localization. Although a resolution of 0.5 km clearly captures shear zone development in the reference model and in previous outer-rise studies [*Faccenda et al*., 2008, 2009], increasing the resolution of the reference model to 0.25 km does influence faulting patterns and individual shear zones. Specifically, at the higher resolution (0.25 km) shear zones narrow (i.e., more refined localization), the number of faults increases and the fault spacing decreases. While the effects of resolution should be noted, a time average of the faulting patterns reveals that values (lateral faulting extent, number of faults, fault spacing) from the two resolutions fall within the standard deviations. Furthermore, testing of additional models revealed that faulting trends associated with varying brittle rheology were unaffected by increasing the resolution. Consequently, the trends observed in the reference model and those discussed below are not a byproduct of poorly resolved shear zone formation and development.

3.2. Plate Structure and Velocity

[29] Given the factors controlling outer-rise faulting patterns within a single model, we now consider the effects of plate age and velocity. Analysis of these models considers time averaged faulting properties, in contrast to the faulting data in Figure 4. As the overriding plate dynamics and slab evolution of each model with a specific plate age or applied velocity will differ with time, we stop our faulting analysis of each model when the trench retreats to a distance of 1375 km. While this condition certainly does not remove all effects of varying dynamics between models, it restricts the time-averaged faulting patterns of each model to similar regimes of overriding plate evolution.

3.2.1. Plate Age

[30] The age of subducting oceanic lithosphere controls the thickness, associated integrated strength and bending resistance of the plate, which in turn directly influences the stresses generated during bending. Consequently, a direct correlation between plate age and faulting patterns is expected as the magnitude of bending stresses and broader slab dynamics varies. Indeed, varying the age of the downgoing oceanic lithosphere from 10 to 140 Myr generates systematic changes in faulting patterns (Figures 5 and 6). For maximum fault viscosities of 10^{23} and 5×10^{22} Pa s, the lateral faulting extent and number of faults both systematically increase as the plate age increases from 10 to 80 Myr (Figures 6a and 6b), but stay roughly constant between 80 and 140 Myr. In contrast, fault spacing only increases significantly from 10 to 30 Myr and is effectively constant from 30 to 80 Myr (Figure 6c) for a maximum fault viscosity of 10^{23} Pa s. Above 80 Myr, however, the fault spacing does show a consistent increase through 140 Myr. The maximum depth of faulting, defined as the last occurrence of viscosity 5×10^{23} Pa s at the

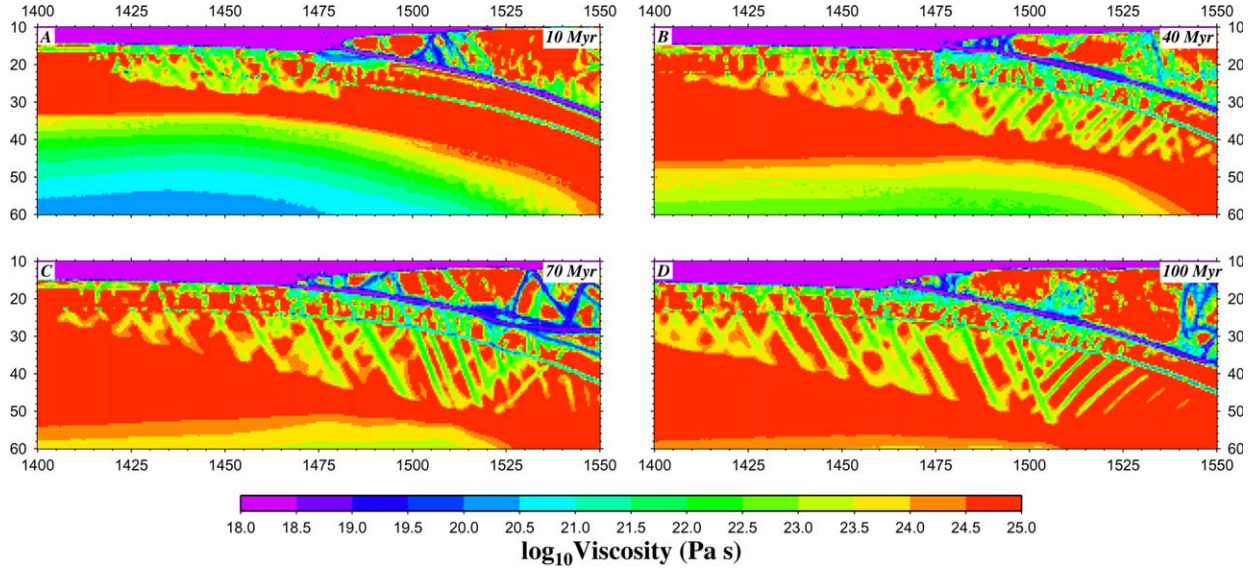

Figure 5. Viscosity structure of deforming oceanic lithosphere and sedimentary accretionary wedge for oceanic plate ages of (a) 10, (b) 40, (c) 70, and (d) 100 Myr, shown at similar horizontal (*x* axis) trench positions. Faulting patterns are strongly sensitive to the age of the downgoing oceanic plate, with faulting extent and depth increasing with downgoing plate age.

horizontal position of the trench, increases with plate age (Figure 6d) from ~ 28 km at 10 Myr to ~ 44 km at 140 Myr.

[31] As with the number and extent of faulting, bending radius values increase with plate age (Figure 6e). The rate of time-averaged bending radius

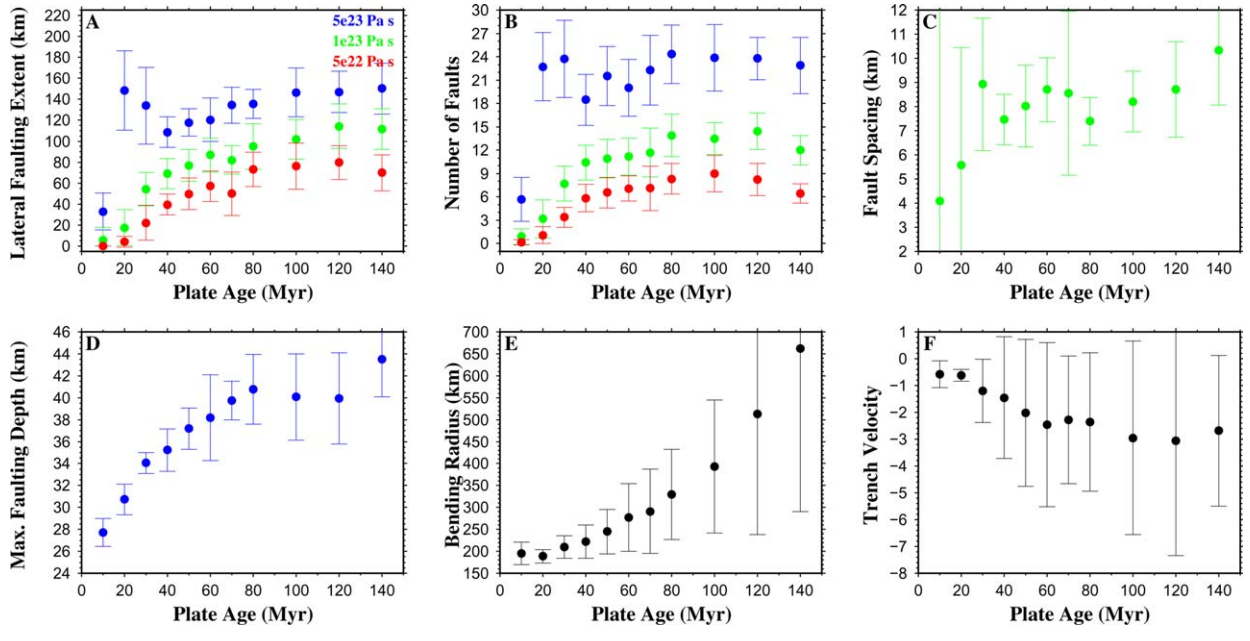

Figure 6. Faulting patterns and downgoing plate dynamics as a function of subducting plate age for an applied velocity of 3.5 cm yr^{-1}. Measurements of (a) lateral faulting extent, (b) the number of faults, (c) fault spacing, (d) maximum faulting depth, (e) bending radius, and (f) trench velocity represent the time-averaged value of each model. Measurements of lateral faulting extent and the number of faults are shown for maximum fault viscosities of 5×10^{23}(blue), 1×10^{23} (green) and 5×10^{22} Pa s (red). The maximum faulting depth is defined as the deepest location with a viscosity 5×10^{23} (Pa s) at the horizontal position of the trench. Measurements of bending radius and trench velocity are independent of viscosity. Error bars represent the standard deviation of each measurement.

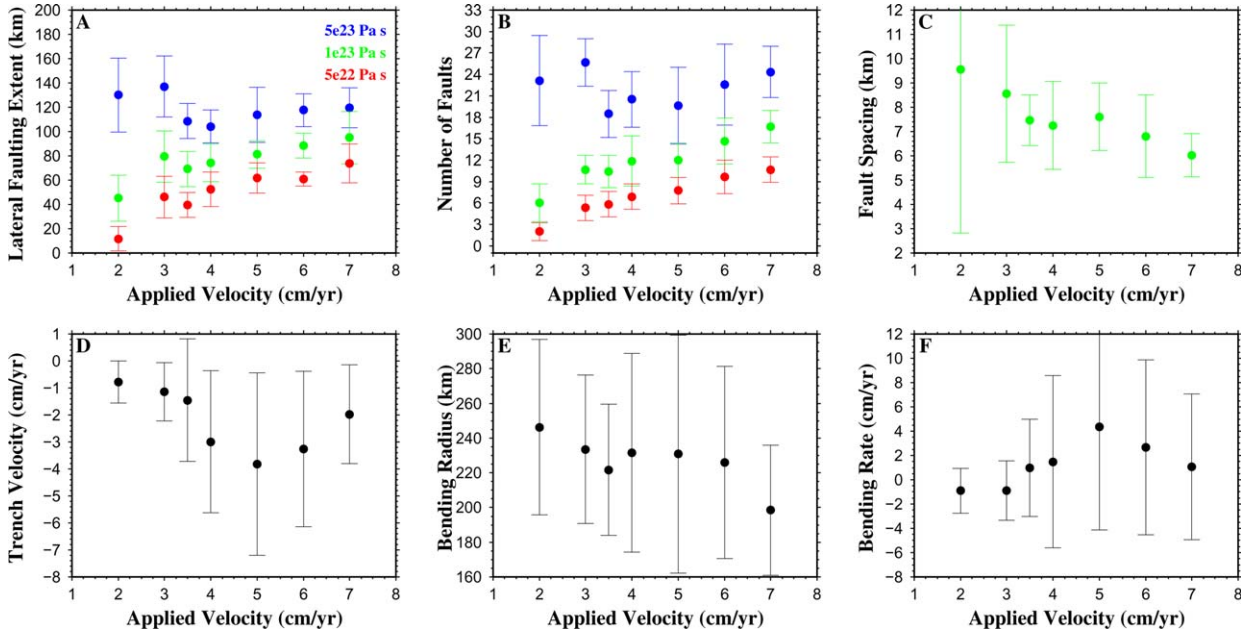

Figure 7. Faulting patterns and downgoing plate dynamics as a function of applied velocity for a subducting plate age of 40 Myr. As in figure 6, each measurement represents the time-averaged value of each model. (a) Lateral faulting extent, (b) number of faults, (c) fault spacing, (d) bending radius, and (e) bending rate.

increase, however, accelerates with increasing plate age, which largely reflects the thicker slabs initial resistance to bending (bending radius $>$ 1000 km) during the early stages of subduction and weakening. In contrast, trench velocity mimics faulting pattern trends, with no significant variations observed past 50 Myr (Figure 6f). Although the magnitude of slab pull also increases with downgoing plate age, its effect on faulting patterns is likely minimal due to the shallow model base depth. Consequently, variations in faulting patterns with increasing plate age largely reflect the associated increase in integrated plate strength and bending resistance.

3.2.2. Applied Velocity

[32] As with plate age, faulting patterns are predicted to vary with plate velocity due to increases or decreases in the rate of slab deformation and flow-driven overriding plate extension, with the latter affecting coupling across the plate boundary and trench retreat rates. Increasing the plate velocity from 2 to 7 cm yr^{-1} increases the extent and number of faults within the downgoing oceanic lithosphere (Figure 7). For a velocity of 2 cm yr^{-1}, brittle deformation is dominated by faults with viscosities greater than 10^{23} Pa s (Figures 7a and 7b). As the applied velocity increases from 2 to 4 cm yr^{-1}, the proportion of low-viscosity faults ($< 10^{23}$ Pa s) also increases, while high-viscosity faults ($>10^{23}$ Pa s) decrease. Above 4 cm yr^{-1}, the number and lateral extent of all faults increases as the applied velocity increases. In contrast, fault spacing remains relatively constant across the examined applied velocity space for a maximum fault viscosity of 10^{23} Pa s (Figure 7c).

[33] The increases in faulting number and extent with increasing applied velocity show no correlations to corresponding variations in trench velocity, bending radius or bending rate (Figures 7d and 7f). While variations in trench velocity closely follow the slab bending rate, the bending radius stays roughly constant. Consequently, variations in faulting patterns across the spectrum of applied velocities largely reflect the dependence of bending stresses on the rate at which material passes through zones of curvature.

3.3. Slab Pull

[34] In order to assess the role of slab pull on faulting patterns, we consider models with a base depth of 660 km. Compared to previous models with a 200 km base depth, extending the base depth increases the magnitude of flow in the mantle wedge and drives rapid intra-arc necking and breakup of the overriding plate within. At this point of breakup, the downgoing plate transitions from strongly "coupled" to largely 'uncoupled'

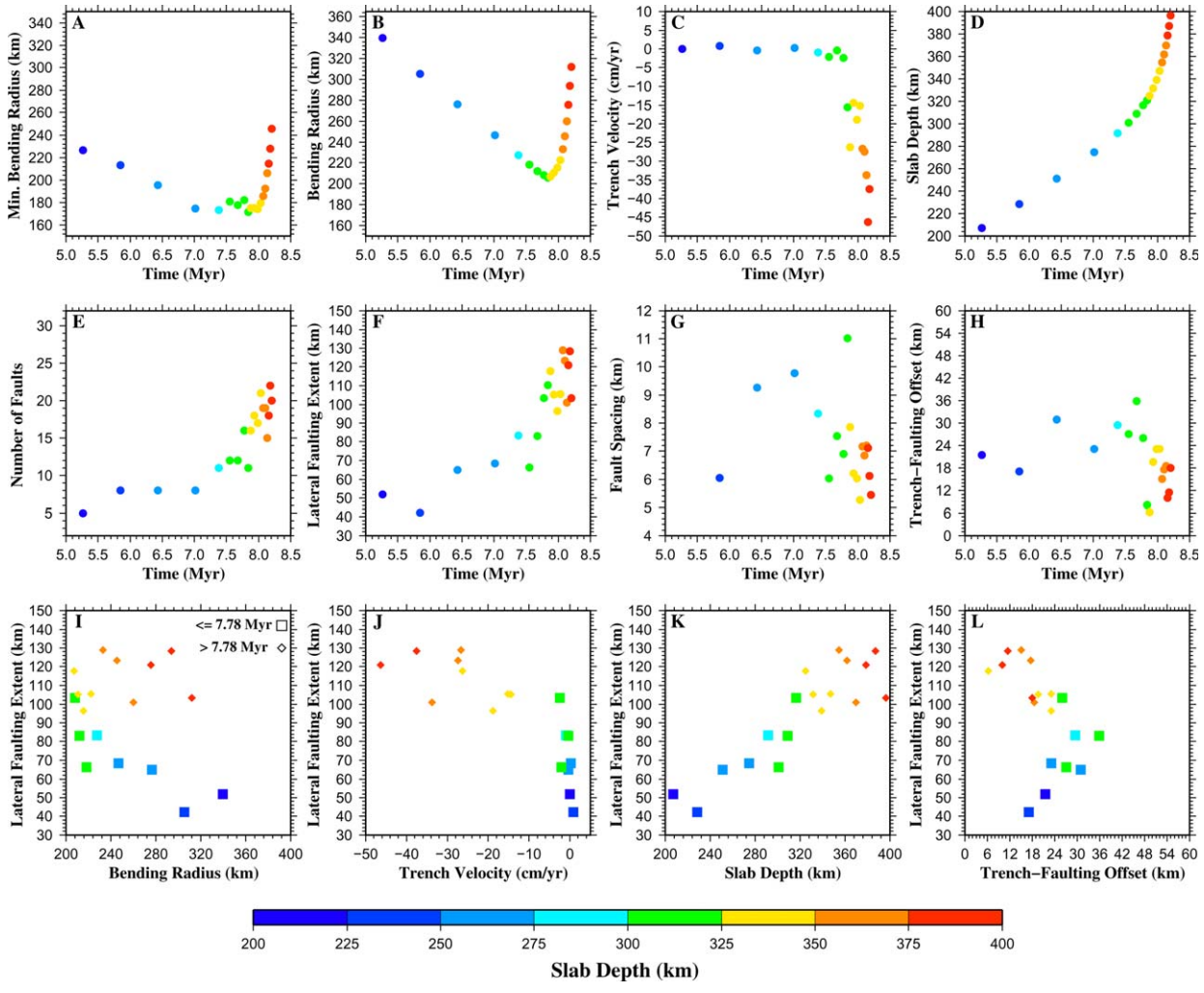

Figure 8. Deep-box model. Top: temporal evolution of the downgoing oceanic lithosphere's (a) minimum bending radius, (b) bending radius, (c) trench velocity, and (d) slab depth. Middle: temporal evolution of (e) the number of faults, (f) lateral faulting extent, (g) fault spacing, and (h) trench-faulting offset in the outer rise. Bottom: lateral faulting extent as a function of (i) bending radius, (j) trench velocity, (k) slab depth, and (l) trench-faulting offset. Each point is colored according to slab depth. A maximum fault viscosity of 5×10^{22} Pa s was used to determine faulting characteristics. Temporal trends in faulting patterns change sharply near 7.78 Myr, when the downgoing-plate largely decouples from the overriding plate.

from the overriding plate. Time sequences of downgoing plate dynamics (Figures 8a and 8e) and faulting behavior (Figures 8e and 8f) illustrate this transition from 'coupled' to 'uncoupled' subduction regimes, which clearly shows the transition occurring just prior to 8 Myr.Prior to the transition, the bending and minimum bending radius systematically decrease (Figures 8a and 8b), but subsequently sharply increase as the slab decouples, begins to roll back rapidly (Figure 8c) and accelerate its descent (Figure 8d). As the slab descends and the magnitude of slab pull increases prior to decoupling, the number of faults and lateral faulting extent both increase (Figures 8e and 8f), while faulting spacing varies significantly and the distance between the trench and last fault stays roughly constant (Figures 8g and 8h). Following the transition to an uncoupled regime, the number and lateral extent of faults increase rapidly (Figures 8e and 8f), while the fault spacing and trench-faulting offset decrease rapidly (Figures 8g and 8h). Notably, fault spacing values vary significantly as a function of time within the coupled regime, but remain tightly clustered within the uncoupled regime.

[35] The distinct slab and faulting behavior between uncoupled and coupled regimes is evident

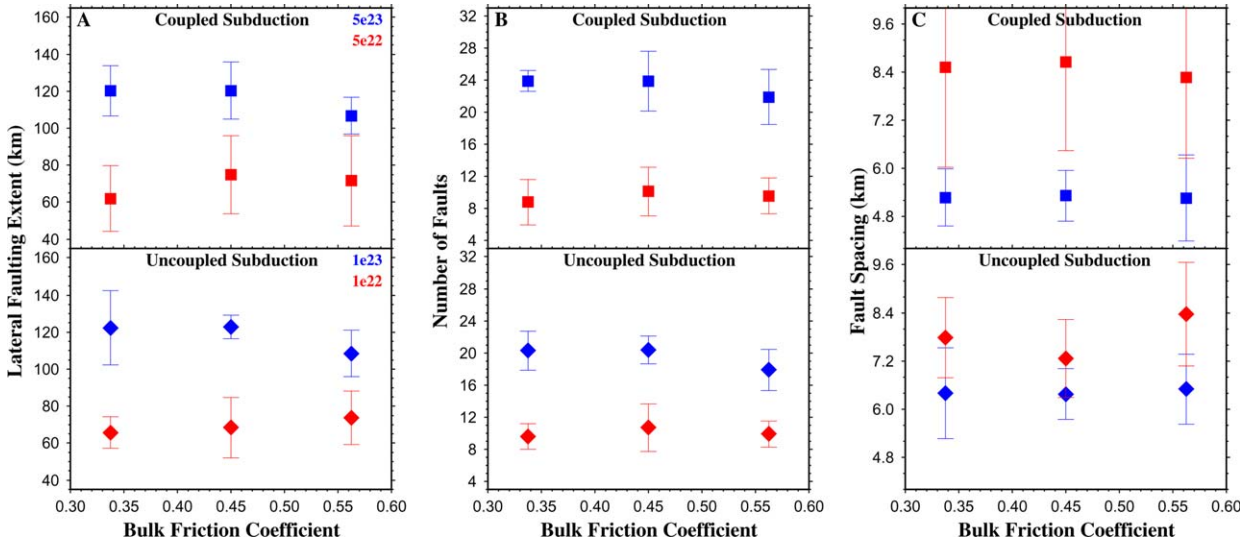

Figure 9. (a) Lateral faulting extent, (b) number of faults, and (c) fault spacing as a function of bulk friction coefficient for deep-box (660 km) models. As in Figure 8, the oceanic plate age is 40 Myr and the applied velocity is 3.5 cm yr^{-1}. Top: coupled subduction regime with maximum fault viscosities of 5×10^{23} (blue) and 5×10^{22} (red) Pa s. Bottom: uncoupled subduction regime with maximum fault viscosities of 10^{23} (blue) and 10^{22} (red) Pa s. Faulting properties are largely insensitive to variations in the bulk friction coefficients.

in the relationships between the lateral faulting extent and bending radius, trench velocity, slab depth and trench-faulting offset (Figures 8i–8l). In the coupled regime ($<$ 7.78 Myr), the lateral faulting extent decreases with increasing bending radius, shows no dependence on trench velocity and increases with increasing slab depth and trench-faulting offset. In the uncoupled regime ($>$ 7.78 Myr), the lateral faulting extent remains constant across a range of bending radius and trench velocity values, but increases with slab depth at a rate similar to that in the uncoupled regime.

3.4. Rheology

[36] The effect of brittle rheology on outer-rise faulting patterns for models with a 660 km base depth is explored through variations in friction coefficient, while holding the plate age & applied velocity constant. The friction coefficient values for the oceanic crust and mantle $(\sin\varphi_{\text{strong}}, \sin\varphi_{\text{weak}})$ are decreased or increased by 25% (or 50%—Figure 9) from reference values $(\sin\varphi_{\text{strong,weak}} = 0.6, 0.3)$ and time-averaged faulting values are plotted against the associated bulk friction coefficient $(\frac{\sin\varphi_{\text{strong}}, \sin\varphi_{\text{weak}}}{2})$ for coupled and uncoupled subduction regimes (Figure 9). The friction coefficient variations of $\pm$25% (or +50%/−25%) are designed to provide a range of values within the bounds of observed friction coefficient values from analysis of abyssal hill faults [*Billen et al.*, 2007].

[37] Faulting patterns are plotted for maximum fault viscosities of 5×10^{23} and 5×10^{22} Pa s (coupled subduction) or 10^{23} and 10^{22} Pa s (uncoupled subduction), which illustrates the expanded (lateral-faulting extent) and enhanced (fault viscosity) deformation in the uncoupled regime. In contrast to the transition in faulting behavior between coupled and uncoupled regimes, a 25% increase or decrease in the brittle strength has little impact on the extent, number or spacing of faults, regardless of the subduction regime or maximum fault viscosity. In order to test the robustness of this finding, we increased the numerical resolution by a factor of 2 (250 m) in the vicinity of the trench and examined a similar range of bulk friction coefficient values. As in Figure 9, time-averaged faulting patterns in the high-resolution models exhibited little to no dependence on variations in the brittle strength of the downgoing plate.

4. Discussion

[38] The results presented here indicate that downgoing plate thickness and velocity, slab pull magnitude and overriding-downgoing plate coupling exert a first order control on outer-rise faulting patterns in oceanic-continental subduction systems. These findings are largely consistent with

numerous previous results that found plate age [e.g., *Capitanio et al*., 2009; *Rose and Korenaga*, 2011; *Buffet and Becker*, 2012], velocity [e.g., *Buffet*, 2006; *Rose and Korenaga*, 2011], slab-pull [e.g., *Capitanio et al*., 2009;] and downgoing-overriding plate coupling [*Gerya and Meilick* 2011; *Tan et al*., 2012] strongly affect the stress state in the bending region of subduction zones. In comparison, faulting patterns exhibit significantly less sensitivity to variations in the brittle strength of the oceanic crust and mantle. The validity of this finding depends, in part, on the fit between calculated and observed outer-rise faulting patterns.

4.1. Comparison to Observations

[39] As discussed in section 3.2.1, the reference model lateral faulting extent and fault spacing fall well within observed global ranges (Table 1), which is also the case for models with different plate ages, downgoing-overriding plate coupling, slab pull magnitudes and applied velocities. Consequently, we are confident that the observed dependence of outer-rise faulting patterns on the studied parameters can be realistically applied to the majority of subduction zones. However, the lack of a clear correlation between plate age, convergence rate, slab-pull and observed faulting patterns (Table 1) suggests that outer-rise deformation may reflect a complicated interdependence on these parameters, or additional factors, such as coupling across the plate-boundary interface and heterogeneous incoming plate-structure also strongly influence outer-rise dynamics.

[40] Indeed, the results of this study (Figures 8 and 9), previous numerical studies [*Gerya and Meilick*, 2011; *Tan et al*., 2012] and seismic analysis of outer-rise earthquake [e.g., *Christensen and Ruff*, 1988; *Massell*, 2002; *Todd and Lay*, 2013] reveal a clear correlation between plate boundary coupling and outer-rise deformation, while incoming plate structure may lead to reactivation of pre-existing faults or a combination of fault reactivation and new fault development [e.g., *Massell*, 2002; *Ranero et al*., 2003; *Oakley et al*., 2008]. When this suite factors is considered, it is not surprising the simplified numerical models in this study reveal outer-rise faulting dependencies that are not discernable in the limited set of outer-rise faulting observations. Consequently, future numerical studies will likely need to focus on specific regions in order to carefully account for the wide range of parameters influencing outer-rise deformation.

4.2. Faulting Patterns and Brittle Strain Weakening

[41] While the results of this study establish clear relationships between outer-rise deformation and numerous components of subduction dynamics, it is important to distinguish why variations in the brittle strength of the oceanic lithosphere in this study exert comparatively less influence than in previous studies of extensional systems. In particular, numerical modeling of continental extensional [e.g., *Buck et al*., 2003; *Moresi and Muhlhaus*, 2006] commonly reveals that increasing the magnitude of brittle strain weakening (i.e., difference between $sin\varphi_{weak}$ d$sin\varphi_{strong}$ eads to wider fault spacing. Similarly, increasing the magnitude of brittle strain weakening in extending oceanic lithosphere increases fault spacing in both boundary condition-driven [*Supak et al*., 2006] and dynamic [*Faccenda et al*., 2009] models of bending. Here, no clear, quantitative increases in time-dependent fault spacing occur with increasing brittle weakening.

[42] It should be noted, however that the physics and dynamics of bending-related extension notably differs from common lithospheric extension settings in that material points of the downgoing slab are continuously passing through the relatively stationary extensional zone. Consequently, the lack of clear, quantitative time-dependent fault spacing trends with varying strain weakening largely reflects the strong time-dependent variations in the stress field driving deformation. In the studies above, with the exception of *Faccenda et al*. [2009], extension is driven by boundary conditions such that the large-scale stress and strain-rate fields are relatively constant through time. Consequently, variations in the brittle rheology are clearly expressed.

[43] In this study, deformation in the outer-rise region reflects both the rheology and changes in the background stress and strain-rate fields, which are largely driven by changes in the overriding plate dynamics and slab pull (deep-box models only) within a single model. Simply put, time-dependent changes to the large-scale stress and strain-rate fields in the outer-rise region modify faulting patterns significantly more than the examined variations in rheology. This is supported by the strong modification of faulting patterns by variations in plate thickness, applied velocity, slab pull and downgoing-overriding plate coupling, which directly influence the stress and strain-rate fields driving deformation.

[44] It is important to note, however, that the outer-rise experiments of *Faccenda et al*. [2009] produce clearer faulting pattern trends with varying amounts of strain weakening, while using a similar numerical setup and the same code. The differences between trends in this study and those in *Faccenda et al*. [2009] reflect a number of factors. Most importantly, *Faccenda et al*. [2009] examined an oceanic-oceanic subduction system, where the overriding plate did not undergo extension and breakup through time. As a result, the large-scale stress field in the outer-rise region experienced significantly less time-dependent variations due to downgoing-overriding plate coupling and back-arc extension.

[45] In addition, the experiments of *Faccenda et al*. [2009] included elasticity, which modifies fault spacing through the ratio between the elastic bulk modulus and lithostatic pressure [*Cundall*, 1990; *Buiter et al*., 2006]. While further testing will be needed to determine how much elasticity affects outer-rise deformation, the consistently smaller faulting spacing (2–3 km) in *Faccenda et al*. [2009] likely reflects elastic effects. The presence of free-water particles in the outer-rise region in *Faccenda et al*. [2009] may also slightly influence fault spacing, although they are likely to have a much stronger influence on the magnitude of viscous weakening within individual faults.

[46] In future studies, examining the role of rheology on outer-rise faulting patterns, efforts will need to focus on specific regions in order to fully or partially constrain the magnitude of slab pull, plate age, plate velocity, and downgoing-overriding plate coupling. Constraining these parameters will allow a closer examination of how brittle rheology, downgoing plate heterogeneity, and fluid transport affect faulting patterns. Candidates for targeted regional studies include Japan, Central and South America, Alaska, and Tonga-Kermadec due to the excellent constraints on both regional slab structure and outer-rise faulting patterns.

5. Conclusions

[47] Modeling of visco-plastic deformation in an oceanic-continental subduction system indicates that downgoing plate thickness and velocity, downgoing-overriding plate coupling and the magnitude of slab pull exert a first-order influence on faulting patterns in the outer-rise region. In particular, the depth and lateral extent of the faulting area as well as the number of faults in it positively correlate with both the plate age and subducting plate velocity. Stabilization of the faulting pattern parameters is documented for relatively old (>80 Myr) slabs. Comparatively, the brittle rheology and connate water content of the downgoing oceanic lithosphere exerts significantly less influence on faulting patterns. This characteristic suggests that for the range in friction and water parameters tested, outer-rise faulting patterns are largely controlled by the overall stress-state and rate of deformation within subduction systems. While time-averaged measurements of fault spacing and lateral faulting extent fall within the range of global observations, direct comparisons to specific regions are difficult due to the strong influence of multiple physical parameters on faulting patterns and the wide range of faulting patterns observed within individual subudction zones. Future models of outer-rise deformation should incorporate regional-specific estimates of incoming plate structure, down-dip slab structure and overriding plate characteristics in order to carefully explore the relative contributions of subduction dynamics, brittle rheology and fluid transport to outer-rise faulting patterns.

Acknowledgments

[51] This work was supported by the U.S. National Science Foundation under grants EAR-1049660 (M.I.B.) and EAR-0748818 (M.I.B.). Lengthy discussions with Larry Ruff and thorough reviews from Clint Conrad, Fabio Capitanio, and an anonymous reviewer greatly improved the manuscript.

References

Alisic, L., M. Gurnis, G. Stadler, C. Burstedde, and O. Ghattas (2012), Multi-scale dynamics and rheology of mantle flow with plates, *J. Geophys. Res.*, *117*, B10402, doi:10.1029/2012JB009234.

Arredondo, K. M., and M. I. Billen (2012), Rapid weakening of subducting plates from trench-parallel estimates of flexural rigidity, *Phys. Earth Planet. Inter.*, *196–197*, 1–13.

Becker, T. W., C. Faccena, R. J. O'Connell, and D. Giardini (1999), The development of slabs in the upper mantle: Insights from numerical and laboratory experiments, *J. Geophys. Res.*, *104*(B7), 15,207–15,226.

Billen, M., E. Cowgill, and E. Buer (2007), Determination of fault friction from reactivation of abyssal-hill faults in subduction zones, *Geology*, *35*(9), 819–822, doi:10.1130/G23847A.1.

Billen, M. I., and M. Gurnis (2005), Constraints on subducting plate strength within the Kermadec trench, *J. Geophys. Res.*, *110*, B05407, doi:10.1029/2004JB003308.

Buck, W. R., L. L. Lavier, and A. Babeyko (2003), A numerical model of lithospheric extension producing fault-bounded basins and ranges, *Int. Geol. Rev.*, *45*, 712–723.

Buffett, B. A. (2006), Plate force due to bending at subduction zones, *J. Geophys. Res.*, *111*, B09405, doi:10.1029/2006JB004295.

Buffett, B. A., and T. W. Becker (2012), Bending stress and dissipation in subducted lithosphere, *J. Geophys. Res.*, *117*, B05413, doi:10.1029/2012JB009205.

Buiter, S. J. H., A. Y. Babeyko, S. Ellis, T. V. Gerya, B. J. P. Kaus, A. Kellner, G. Schreurs, and Y. Yamada (2006), The numerical sandbox: comparison of model results for a shortening and an extension experiment, *Geol. Soc. London Spec. Publ.*, *253*, 1–27.

Capitanio, F. A., G. Morra, and S. Goes (2007), Dynamic models of downgoing plate-bouyancy driven subduction: Subduction motions and energy dissipation, *Earth Planet. Sci. Lett.*, *262*, 284–297.

Capitanio, F. A., G. Morra, and S. Goes (2009), Dynamics of plate bending at the trench and slab-plate coupling, *Geochem. Geophys. Geosyst.*, *10*, Q04002, doi:10.1029/2008GC002348.

Christensen, D. H., and L. J. Ruff (1988), Seismic coupling and outer rise earthquakes, *J. Geophys. Res.*, *93*(B11), 13,421–13,444.

Connolly, J. A. D. (2005), Computation of phase equilibria by linear programming: A tool for geodynamic modeling and its application to subduction zone decarbonation, *Earth Planet. Sci. Lett.*, *236*, 524–541.

Conrad, C. P., and B. H. Hager (1999), Effects of plate bending and fault strength at subduction zones on plate dynamics, *J. Geophys. Res.*, *104*(B8), 17,551–17,571.

Conrad, C. P., and B. H. Hager (2001), Mantle convection with strong subduction zones, *Geophys. J. Int.*, *144*, 271–288.

Conrad, C. P., and C. Lithgow-Bertelloni (2002), How mantle slabs drive plate tectonics, *Science*, *298*(5591), 207–209.

Contreras-Reyes, E., and A. Osses (2010), Lithospheric flexure modeling seaward of the Chile trench: implications for oceanic plate weakening in the trench outer rise region, *Geophys. J. Int.*, *182*(1), 97–112.

Cundall, P. A. (1990), Numerical modeling of jointed and faulted rock, in *Mechanics of Jointed and Faulted Rocks*, edited by A. Rossmanith, pp. 11–18, A. A. Balkema, Rotterdam.

De Bremaecker, J.-C. (1977), Is the oceanic lithosphere elastic or viscous?, *J. Geophys. Res.*, *82*(14), 2001–2004.

Di Giuseppe, E., van Hunen, J., Funiciello, F., Faccenna, C. and D. Giardini (2008), Slab stiffness control of trench motion: Insights from numerical models, *Geochem. Geophys. Geosyst.*, *9*, Q02014, doi:10.1029/2007GC001776.

Escartin, J., G. Hirth, and B. Evans (1997a), Effects of serpentinization on the lithospheric strength and the style of normal faulting at slow-spreading ridges, *Earth Planet. Sci. Lett.*, *151*(3–4), 181–189.

Faccenda, M., L. Burlini, T. V. Gerya, and D. Mainprice (2008), Fault-induced seismic anisotropy by hydration in subducting oceanic plates, *Nature*, *455*(7216), 1097–1100.

Faccenda, M., T. V. Gerya, and L. Burlini (2009), Deep slab hydration induced by bending-related variations in tectonic pressure, *Nat. Geosci.*, *2*(11), 790–793.

Floyd, J. S., J. C. Mutter, A. M. Goodliffe, and B. Taylor (2001), Evidence for fault weakness and fluid flow within an active low-angle normal fault, *Nature*, *411*(6839), 779–783.

Gerya, T. V., and F. I. Meilick (2011), Geodynamic regimes of subduction under an active margin: Effects of rheological weakening by fluids and melts, *J. Metamorphic Geol.*, *29*, 7–31, doi:10.1111/j.1525-1314.2010.00904.x.

Gerya, T. V., and D. A., Yuen (2003a), Characteristics-based marker-in-cell method with conservative finite-differences schemes for modeling geological flows with strongly variable transport properties, *Phys. Earth Planet. Inter.*, *140*, 295–320.

Gerya, T. V., and D. A. Yuen (2003b), Rayleigh-Taylor instabilities from hydration and melting propel ''cold plumes'' at subduction zones, *Earth Planet. Sci. Lett.*, *212*, 47–62, doi:10.1016/S0012–821X(03)00265-6.

Gerya, T. V., and D. A. Yuen (2007), Robust characteristics method for modeling multiphase visco-elasto-plastic thermo-mechanical problems, *Phys. Earth Planet. Inter.*, *163*, 83–105, doi:10.1016/j.pepi.2007.04.015.

Gerya, T. V., J. A. D., Connolly, D. A. Yuen, W. Gorczyk, and A. M. Capel (2006), Seismic implications of mantle wedge plumes, *Phys. Earth Planet. Inter.*, *156*, 59–74.

Gorczyk, W., A. P. Willner, T. V. Gerya, J. A. D. Connolly, and J.-P. Burg (2007), Physical controls of magmatic productivity at Pacific-type convergent margins: numerical modeling, *Phys. Earth Planet. Inter.*, *163*, 209–232.

Grevemeyer, I., N. Kaul, J. L. Diaz-Naveas, H. W. Villinger, C. R. Ranero, and C. Reichert (2005), Heat flow and bending-related faulting at subduction trenches: Case studies offshore of Nicaragua and central Chile, *Earth Planet. Sci. Lett.*, *236*(1–2), 238–248, doi:10.1016/j.epsl.2005.04.048.

Grevemeyer, I., C. R. Ranero, E. R. Flueh, D. Klschen, and J. Bialas (2007), Passive and active seismological study of bending-related faulting and mantle serpentinization at the Middle America trench, *Earth Planet. Sci. Lett.*, *258*(3–4), 528–542, doi:10.1016/j.epsl.2007.04.013.

Hilde, T. W. C. (1983), Sediment subduction versus accretion around the Pacific, *Tectonophysics*, *99*(2-4), 381–397.

Hirth, G., and D. Kohlstedt (1996), Water in the oceanic upper mantle: implications for rheology, melt extraction and the evolution of the lithosphere, *Earth Planet. Sci. Lett.*, *144*, 93–108.

Ivandic, M., I. Grevemeyer, J. Bialas, and C. Joerg Peterson (2010), Serpentinization in the trench-outer rise region offshore of Nicaragua: Constraints from seismic refraction and wide-angle data, *Geophys. J. Int.*, *180*, 1253–1264, doi:10.1111/j.1365-246X.2009.04474.x.

Jones, G., T. Hilde, G. Sharman, and D. Agnew (1978), Fault patterns in outer trench walls and their tectonic significance, *J. Phys. Earth*, *26*, suppl. P S85–S101.

Key, K., S. Constable, T. Matsuno, R. L. Evans, and D. Myer (2012), Electromagnetic detection of plate hydration due to bending faults at the Middle America Trench, *Earth Planet. Sci. Lett.*, *351–352*, 45–53.

Kobayashi, K., M. Nakanishi, K. Tamaki, and Y. Ogawa (1998), Outer slope faulting associated with the western Kuril and Japan trenches, *Geophys. J. Int.*, *134*(2), 356–372, doi:10.1046/j.1365-246x.1998.00569.x.

Lallemand, S., A. Heuret, and D. Boutelier (2005), On the relationships between slab dip, back-arc stress, upper plate absolute motion, and crustal nature in subduction zones, *Geochem. Geophys. Geosyst.*, *6*, Q09006, doi:1029/2005GC000917.

Lefeldt, M., C. R. Ranero, and I. Grevermeyer (2012), Seismic evidence of tectonic control on the depth of water influx into incoming oceanic plates at subduction trenches, *Geochem. Geophys. Geosyst.*, *13*, Q05013, doi:1029/2012GC004043.

Leng, W., and S. Zhong (2010), Constraints on viscous dissipation of plate bending from compressible mantle convection, *Earth Planet. Sci. Lett.*, *297*, 154–164.

Ludwig, W., J. I. Ewing, M. Ewing, S. Murauchi, N. Den, S. Asano, H. Hotta, M. Hayakawa, T. Asanuma, K. Ichikawa,

and I. Noguchi (1966), Sediments and structure of the Japan trench, *J. Geophys. Res.*, *71*(8), 2121–2137.

Lynnes, C. S., and T. Lay (1988), Source process of the great 1977 Sumba earthquake, *J. Geophys. Res.*, *93*(B11), 13,407–13,420.

Massell, C. (2002), Large-scale structural variation of trench outer slopes and rises, Ph.D. thesis, Univ. of Calif., San Diego, Calif.

Masson, D. G. (1991), Fault patterns at outer trench walls, *Mar. Geophys. Res.*, *13*(3), 209–225.

Melosh, H. (1978), Dynamic support of the outer rise, *Geophys. Res. Lett.*, *5*(5), 321–324.

Moresi, L., and H.-B. Muhlhaus (2006), Anistropic viscous models of large-deformation Mohr-Coulomb failure, *Philos. Mag.*, *86*(21–22), 3287–3305.

Mortera-Gutierrez, C. A., D. W. Scholl, and R. L. Carlson (2003), Fault trends on the seaward slope of the Aleutiona Trench: Implications for a laterally changing stress field tied to a westward increase in oblique convergence, *J. Geophys. Res.*, *108*(B10), 2477, doi:10.1029/2001B001433.

Nikolaeva, K., Gerya, T. V., and F. O. Marques (2010), Subduction initiation at passive margins: Numerical modeling, *J. Geophys. Res.*, *115*, B03406, doi:10.1029/2009JB006549.

Oakley, A. J., B. Taylor, and G. F. Moore (2008), Pacific Plate subduction beneath the central Mariana and Izu-Bonin fore arcs: New insights from an old margin, *Geochem. Geophys. Geosyst.*, *9*, Q06003, doi:1029/2007GC001820.

Parsons, B., and P. Molnar (1976), The origin of outer topographic rises associated with trenches, *Geophys. J. R. Astron. Soc.*, *45*, 707–712.

Ranero, C. R., and V. Sallares (2004), Geophysical evidence for hydration of the crust and mantle of the Nazca plate during bending at the north Chile trench, *Geology*, *32*(7), 549–552, doi:10.1130/G20379.1.

Ranero, C. R., J. P. Morgan, K. McIntosh, and C. Reichert (2003), Bending-related faulting and mantle serpentinization at the Middle America trench, *Nature*, *425*(6956), 367–373.

Ranero, C. R., A. Villasenor, J. P. Morgan, and W. Weinrebe (2005), Relationship between bend-faulting at trenches and intermediate-depth seismicity, *Geochem. Geophys. Geosyst.*, *6*, Q12002, doi:10.1029/2005GC000997.

Rose, I. R., and J. Korenaga (2011), Mantle rheology and the scaling of bending dissipation in plate tectonics, *J. Geophys. Res.*, *99*, B06404, doi:10.1029/2010JB008004.

Schellart, W. P. (2009), Evolution of the slab bending radius and the bending dissipation in three-dimensional subduction models with a variable slab to upper mantle viscosity ratio, *Earth Planet. Sci. Lett.*, *288*, 309–319.

Schmeling, H., et al. (2008), A bench-mark comparison of spontaneous subduction models—Towards a free surface, *Phys. Earth Planet. Inter.*, *171*, 198–223.

Stadler, G., Gurnis, M., Burstedde, C., Wilcox, L. C., Alisic, L., and O. Ghattas (2010), The dynamics of plate tectonics and mantle flow: From local to global scales, *Science*, *329*, 1033–1038.

Supak, S., D. R. Bohnenstiehl, and W. R. Buck (2006), Flexing is not stretching: An analogue study of flexure-induced fault populations, *Earth Planet. Sci. Lett.*, *246*, 125–137.

Syracuse, E. M., G. A. Abers, K. Fischer, L. MacKenzie, C. Rychert, M. Protti, V. Gonzlez, and W. Strauch (2008), Seismic tomography and earthquake locations in the Nicaraguan and Costa Rican upper mantle, *Geochem. Geophys. Geosyst.*, *9*, Q07S08, doi:10.1029/2008GC001963.

Tan, E., Lavier, L. L., Van Avendonk, H. J. A., and A. Heuret (2012), The role of frictional strength on plate coupling at the subduction interface, *Geochem. Geophys. Geosyst.*, *13*, Q10006, doi:10.1029/2012GC004214.

Tilmann, F. J., I. Grevemeyer, E. R. Flueh, T. Dahm, and J. Gofller (2008), Seismicity in the outer rise offshore southern Chile: Indication of fluid effects in crust and mantle, *Earth Planet. Sci. Lett.*, *269*(1-2), 41–55.

Todd, E. K., and T. Lay (2013), The 2011 Northern Kermadec earthquake doublet and subduction zone faulting interactions, *J. Geophys. Res.*, *118*, 249–261, doi:10.1029/2012JB009711.

Turcotte, D. L., and G. Schubert (2002), *Geodynamics*, 2nd ed., Cambridge Univ. Press, Cambridge, U. K.

Turcotte, D. L., D. C. McAdoo, and J. G. Caldwell (1978), An elastic-perfectly plastic analysis of the bending of the lithosphere at a trench, *Tectonophysics*, *47*(3–4), 193–205.

van Summeren, J., C.P. Conrad, and C. Lithgow-Bertelloni (2012), The importance of slab pull and a global asthenosphere to plate motions, Geochem. Geophys. Geosyst., 13, Q0AK03, doi:10.1029/2011GC003873.

Vogt, K., T. V. Gerya, and A. Castro (2012), Crustal growth at active continental margins: Numerical modeling, *Phys. Earth Planet. Inter.*, *192–193*, 1–20.

Wu, B., C. P. Conrad, A. Heuret, C. Lithgow-Bertelloni, and S. Lallemand (2008), Reconciling strong slab pull and weak plate bending: The plate motion constraint on the strength of mantle slabs, *Earth Planet. Sci. Lett.*, *272*, 412–421.